

Static response and stability of coated microbubbles—multiplicity of solutions and parameter estimation

This content has been downloaded from IOPscience. Please scroll down to see the full text.

2014 Fluid Dyn. Res. 46 041422

(<http://iopscience.iop.org/1873-7005/46/4/041422>)

View [the table of contents for this issue](#), or go to the [journal homepage](#) for more

Download details:

IP Address: 195.251.17.172

This content was downloaded on 21/07/2014 at 08:28

Please note that [terms and conditions apply](#).

Static response and stability of coated microbubbles—multiplicity of solutions and parameter estimation

Alkmini Lytra and Nikos Pelekasis

Department of Mechanical Engineering, University of Thessaly, Pedion Areos, Volos 38334, Greece

E-mail: pel@uth.gr

Received 14 November 2013, revised 9 March 2014

Accepted for publication 1 April 2014

Published 17 July 2014

Communicated by H J Sung and M Brons

Abstract

The static response of a coated microbubble subject to an external pressure distribution is investigated, in order to identify different response patterns with varying viscoelastic properties of the shell. Theoretical and numerical analysis of the axisymmetric response of a microbubble is performed via the static force balance, in order to obtain the radial and tangential (polar) displacements of a shell subject to a uniform or point load. The stretching and bending stiffnesses of the shell, along with the compressibility of the internal gas, comprise the resistance to deformation of the microbubble. The finite element methodology, with B-splines as basis functions, is employed for the solution of the nonlinear static problem while Newton's iterations provide the converged solution. The Jacobian matrix provides necessary information regarding stability of the emerging static configurations. The buckling instability of a uniformly loaded shell results in a subcritical bifurcation that is characterized by symmetric/asymmetric shapes for the parameter range pertaining to polymeric/phospholipid shells. As the relative importance of bending stiffness with respect to stretching decreases symmetric shapes determine the primary buckling instability. Strain softening shell behavior conforms to this pattern due to the increase of the effective area dilatation modulus during compression. Increasing the resistance to compression forces the asymmetric and symmetric solution families to terminate at larger bubble volumes. When a point load is considered the force deformation curve is characterized by a transition from a linear Reissner-type to a nonlinear Pogorelov-type response, followed by a regime where resistance to compression dominates. Identifying these regimes in atomic force microscopy measurements can be used for estimating the area dilatation and bending modulus of the shell.

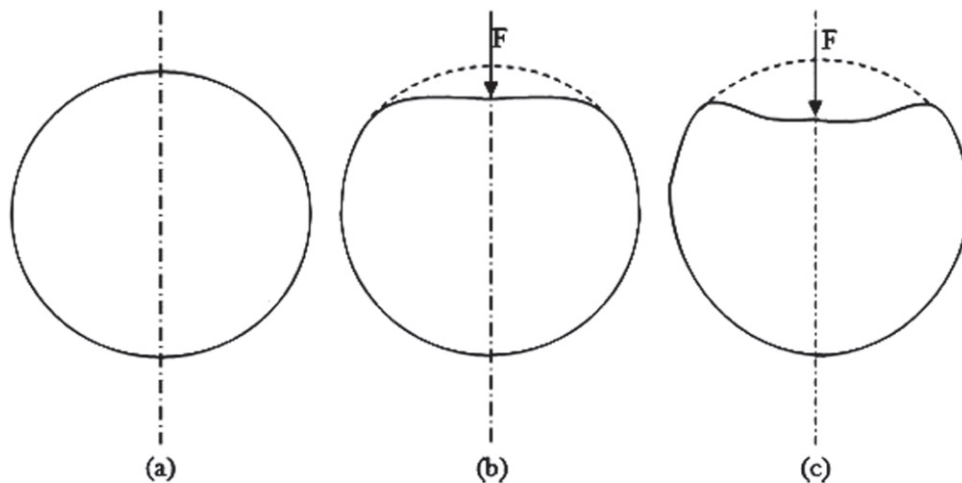


Figure 1. Schematic diagram of deformed microbubble corresponding to increasing external load; (a) spherical shape, (b) flattened around the pole, (c) crater formation.

1. Introduction

Static buckling of spherical shells subject to uniform [1] or distributed [2] external pressure loads has received significant attention in the past in the context of relatively large shells, on the order of several mm and larger, that obey Hooke's law and whose bending moments depend linearly on deviations from the initial curvature. Stability analysis of a uniformly loaded shell recovers static buckling of an initially spherical shape into an axisymmetric post-buckling state that is asymmetric with respect to the equatorial plane [3]. The bifurcating branch is linearly unstable and evolves towards external overpressures that are lower than the critical load, corresponding to a subcritical bifurcation. Consequently, transition to such static shapes from the initial spherical configuration, in the above parameter range, requires a certain level of initial shape deformation, also called imperfection [3]. When a point load distribution is considered, figure 1, the shell originally acquires a flattened shape in the vicinity of the applied load and the force–displacement curve exhibits a linear relationship [4]. As the external load increases dimple formation takes place in the region around the point load and the force–displacement curve exhibits a nonlinear relationship [5]. In both the above regimes stretching and bending resistance control shell deformation, with bending being concentrated in the vicinity of the point load in the 'Reissner' regime whereas dimple formation at the edges of the crater controls bending resistance in the 'Pogorelov' regime. Furthermore, since bending and stretching stiffness are related via the shell thickness, which, in most cases, is a known geometric parameter of the shell, obtaining a force displacement curve, for example via atomic force microscopy (AFM) measurements [6], can provide the shell shear modulus by concentrating on the linear response part where Reissner's linear law holds.

Coated microbubbles, also known as contrast agents, have emerged as powerful contrast enhancers in medical imaging via ultrasound [7] and as drug and gene delivery vectors [8] with highly localized impact on selected tissue. Their viscoelastic coating plays a central role in stabilizing them against dissolution while adding targeting ligands along with an extra oil layer dissolving the therapeutic agent allows for efficient targeting and drug release [8, 9] near

specific tissue where therapeutic treatment is required. Sonication provides the means to control the dynamic response of the microbubbles. To this end two major families of coated microbubbles are normally employed [8], namely those coated by polymeric and phospholipid shells. The former type shells are characterized by larger elasticity modulus hence they are identified as ‘hard’, whereas the latter are characterized by relatively smaller elasticity modulus and a thinner shell hence they are identified as ‘soft’ and more deformable shells. Phospholipid shells are also more amenable to chemical treatment so that they can be attached to neighboring tissue and consequently are better suited for drug delivery applications [9].

In the context of coated microbubbles the static responses mentioned in the penultimate paragraph need to be qualified in order to (a) account for the different constitutive laws describing polymeric [10, 12] or phospholipid [11, 12] shells, (b) account for the fact that the shell thickness is not easily recovered due to the small size of the microbubble, radius on the order of a few microns, and (c) take into consideration the added resistance due to the compressibility of the internal gas. In the present study, the radial and polar components of the force balance on the shell–liquid interface are coupled with the adiabatic condition concerning pressure variations of the ideal gas occupying the microbubble interior, in order to provide the deformed shape and internal pressure of the shell. In addition, different constitutive laws are introduced regarding the mechanical behavior of the shell [13, 14]. In particular, the strain softening and strain hardening constitutive laws are considered with the former conforming better with the response of phospholipid shells. In this context, additional dimensionless parameters are needed concerning the degree of softness of the shell and, more importantly, concerning the relative stiffness of the shell and the gas compressibility. These additional parameters are liable to alter the bifurcation diagram regarding the microbubble response to a uniform external load, depending on the relevant parameter range for different kinds of shell material. As will be seen in the present study, via numerically produced bifurcation diagrams, such differences exist between polymeric and phospholipid shells. Such bifurcation diagrams are available in the literature and exhibit quite a rich structure [15], with a distinct effect of the assumption pertaining to the enclosed gas, i.e. constant volume versus constant internal pressure formulation. In fact, transition from one shape family to another can be used to provide estimates of the shell elastic properties, as was seen in [15] where the extent of the indentation rim in the post-buckling state was associated with the bending modulus, and consequently with the elastic modulus of the shell, and in [16] where the wavenumber of three dimensional wrinkles that develop along the azimuthal direction of the interface of deformed axisymmetric shells can also be associated with the shell elastic modulus. In the present study the microbubble is taken to be axisymmetric and undergoing isothermal variations.

In a different context, an external pressure distribution in the form of a point load can be used as a first approximation of the microbubble response during AFM measurements. As was stressed above, analysis of force–displacement curves from AFM measurements, as a means to obtain estimates of shell elasticity, is normally restricted to its linear part where Reissner’s linear law holds. Nevertheless, this approach rests upon prior knowledge of the shell thickness, which is not guaranteed for the kind of shells considered here. Furthermore, especially for very thin phospholipid shells, the shell thickness may not even be a relevant parameter. In this case the bending stiffness of the shell may be used as a primary variable, instead of the shell thickness, along with the stretching stiffness. In this context, there is ambiguity in the registered response of different types of shells or even similar types of shells exposed to cantilevers with varying stiffness. In particular, polymeric shells exhibit a linear force displacement response curve followed by a nonlinear one with the concave part bent downwards [17, 18]. Prior knowledge of the shell thickness allows for an estimate of shell

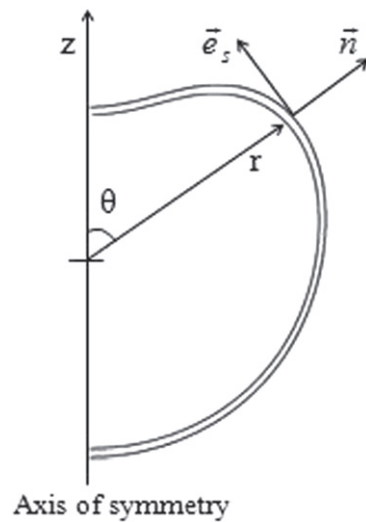


Figure 2. Schematic diagram of a deformed coated microbubble subject to a static load.

elasticity to be obtained, based on the linear part of the response curve which obeys Reissner's law [17]. However, AFM measurements of polymeric shells have also indicated instabilities and multiplicity in the force–displacement response curves for shells of the same microbubble and cantilever size and same shell material. In that case [18], variability in the response curve was also associated with the cantilever stiffness with stiff cantilevers promoting unstable behavior. On the other hand, the response of phospholipid [19], and polyelectrolyte [20], shells is characterized by a transition to nonlinear behavior with the concave part bent upwards. In these cases Reissner's law does not provide a reliable estimate of the shell elastic properties. Resorting to alternative interpretations such as Hertz theory [19], originally derived for rigid spheres [2], or adopting a force balance that ignores shell stretching [20], does not improve the predictive capabilities of the model. Furthermore, in the above approaches the shell's Young's modulus depends on the shell radius.

In the present study a numerical methodology is developed in order to simulate microbubble response to different load distributions and provide a reliable description of the different regimes in the force–displacement curve. Thus, the shell's elastic properties can be estimated upon proper juxtaposition against theoretical models that hold in the same regime, especially for small displacements. Experimental data can then be analyzed in the same fashion in order to provide shell parameters. In section 2, the axisymmetric problem formulation is presented including the relevant interfacial force balance and pressure variation law of the ideal gas inside the shell. In section 3 the numerical methodology that is used for discretizing the problem is outlined and a benchmark bifurcation diagram is presented describing the response of a Hookean shell [15]. Moreover, in section 4 results are obtained for microbubbles coated with a polymeric or a phospholipid shell, while being subject to a uniform or a point load, and directions towards obtaining reliable estimates based on AFM measurements are prescribed. Finally, in section 5 the main findings of the present study are outlined.

2. Problem formulation

We wish to study the static response of an axisymmetric coated microbubble, figure 2, subject to an external pressure distribution. The coating shell is initially taken to be in a stress free state and the pressure of the enclosed gas equilibrated with the ambient atmospheric pressure, P_A . Shell deformation is effected via the application of an external overpressure distribution. Taking the shell thickness to be small but finite the interfacial force balance contains in plane stresses, $\underline{\tau}$, but also the shear stress resultant, \vec{q} , along the plane that is transverse to the shell/ambient interface [1, 21, 22]:

$$\begin{aligned}\Delta\vec{F} &= \Delta\vec{F}_n\vec{n} + \Delta F_t\vec{e}_s \\ &= -\vec{\nabla}_s \cdot \underline{\mathbb{T}}, \\ \underline{\mathbb{T}} &= \underline{\tau} + \vec{q}\vec{e}_s, \\ \Delta F_t &= 0, \\ \Delta F_n &= P - P_G \\ &= P_A + \Delta P - P_G\end{aligned}\quad (1)$$

The gas enclosed by the shell is assumed to be an ideal gas undergoing an isothermal pressure variation subject to the external forcing:

$$P_G V^\gamma = P_0 V_0^\gamma = \text{constant}, \quad \gamma = 1 \text{ for isothermal variations.} \quad (2)$$

In the present study the microbubble is in a zero pre-stress state before the external overpressure, ΔP is applied. Therefore the initial pressure of the enclosed gas is taken to be the ambient pressure, $P_0 = P_A$; V_0 denotes the bubble volume before application of the external overpressure, ΔP , while V, P_G signify the volume and pressure of the enclosed gas at static equilibrium.

The shear stress resultant is associated with the bending moment stress tensor, which is linearly related to variations in the local curvature via the bending modulus k_B :

$$\begin{aligned}\vec{q} &= \vec{\nabla}_s \cdot \underline{m} \cdot \left(\underline{I} - \vec{n}\vec{n} \right), \\ \underline{m} &= m_s \vec{e}_s \vec{e}_s + m_\phi \vec{e}_\phi \vec{e}_\phi \quad m_s = \frac{k_B}{\lambda_\phi} (K_s + \nu K_\phi), \\ K_s &\equiv \lambda_s k_s - k_s^R,\end{aligned}\quad (3)$$

with m_s, m_ϕ denoting the principal components of the moment tensor along the tangential and azimuthal directions, with respect to the generating curve of the axisymmetric shell, and k_s the principal curvature with respect to the tangential direction. Similar relations apply for the azimuthal components m_ϕ and k_ϕ . Regarding the in plane principal stresses $\underline{\tau} = \tau_s \vec{e}_s \vec{e}_s + \tau_\phi \vec{e}_\phi \vec{e}_\phi$, they are associated with the principal extension ratios, λ_s, λ_ϕ , and the elastic modulus in a way that is intimately related to the constitutive law determining the mechanical behavior of the shell material. In the present study three different laws are considered, namely Hooke's law, the Mooney–Rivlin and the Skalak law, corresponding to Hooke's law, strain softening and strain hardening behavior, respectively [13, 14]. When isotropic loading is considered, $\lambda_s = \lambda_\phi$, the in-plane stresses read for the above three cases as:

$$\tau^H = G^H \frac{1 + \nu_s}{1 - \nu_s} (\lambda^2 - 1), \quad G^H: \text{ surface shear modulus} \quad \nu_s: \text{ surface Poisson ratio} \quad (4a)$$

$$\tau^{MR} = G^{MR} (\lambda^2 - 1) (\lambda^4 + \lambda^2 + 1) \frac{1 + b(\lambda^2 - 1)}{\lambda^6} \quad (4b)$$

$$\tau^{SK} = G^{SK} (\lambda^2 - 1) [1 + C\lambda^2 (\lambda^2 + 1)] \quad (4c)$$

with G^H , G^{MR} , $G^{SK} = Gh$ denoting the surface shell shear modulus, G the standard shear modulus and h the shell thickness; parameters b , C are measures of the shell strain softening or strain hardening behavior. The above set of equations is complemented by the symmetry conditions at the two poles

$$\frac{dr}{d\xi} = \frac{d^2\theta}{d\xi^2} = 0, \quad \theta(\xi = 0) = 0, \quad \theta(\xi = 1) = \pi \quad (5)$$

before it is solved for the radial, r , and polar, θ , coordinates of the deformed state and the internal pressure. In the following ξ denotes a Lagrangian variable that signifies specific particles at the shell interface before and after deformation; $\xi = 0, 1$ correspond to the north and south poles of the microbubble. In addition, three different load distributions are considered in the present study:

$$\Delta P(\xi) = P_{\text{EXT}} \text{ corresponding to a uniform distribution} \quad (6a)$$

$$\Delta P = \delta(\xi) P_{\text{EXT}} \text{ corresponding to a point load} \quad (6b)$$

where δ denotes a delta function: $\delta(\xi) = \begin{cases} 0, & \xi \neq 0 \\ 1, & \xi = 0 \end{cases}$ and

$$\Delta P(\xi) = \frac{3}{2\pi \sin^2 \theta_c} \frac{F}{R_0^2} \left(1 - \frac{\sin^2 \theta}{\sin^2 \theta_c} \right)^{0.5}, \quad (6c)$$

load distribution following Hertz [2].

When the case due to a point load is examined, the center of mass of the microbubble in the direction of the axis of symmetry, z_c , is set to zero in order to avoid a net translation of the shell. In a realistic situation, e.g. when AFM measurements are simulated, the solution obtained in this fashion focuses on deformations in the vicinity of the point load while ignoring the details of the deformation at the opposite end of the shell that rests on a solid substrate.

$$z_c = \iiint_V \vec{r} \cdot \vec{e}_z dV = 0 \quad (6d)$$

When a load distribution is applied (equation (6c)), instead of P_{EXT} the total force is known and the angle of contact between the cantilever and the microbubble, θ_c , is treated as an additional unknown that arises as part of the solution of the full nonlinear problem; R_0 is the initial stress free radius of the microbubble. This particular load distribution was obtained by Hertz in his study of two contacting rigid spheres. In the first two cases P_{EXT} is treated as known, while the total force, F , is calculated as part of the post-processing of the solution.

The energy of the deformed configuration is an important indicator that is employed for the characterization of different solution families. In the deformed states under examination the energy consists of three different components. The stretching energy is associated with changes in the principal directions of the rate of strain tensor on the shell interface and, for a shell that obeys Hooke's law, it assumes the form,

$$E_s = \frac{Eh}{2(1-\nu^2)} \int (e_s^2 + 2\nu e_s e_\phi + e_\phi^2) dA_0 \quad e_i = \frac{1}{2} (\lambda_i^2 - 1) \quad (7a)$$

where e_i denotes the principal strain components, A_0 the shell area in the undeformed configuration, ν the Poisson ratio and E the shell Young's modulus. The latter is related to the shear modulus via the shell response at small displacements for the above constitutive laws:

$$E = 2G^s (1 + \nu_s) = 3G^{MR} = 2G^{SK} (1 + 2C) / (1 + C) \quad (7b)$$

Bending energy is associated with the bending measures of strain, $K_s \equiv \lambda_s k_s - k_s^R$, $K_\phi \equiv \lambda_\phi k_\phi - k_\phi^R$,

$$E_b = \frac{k_b}{2} \int (K_s^2 + 2\nu K_s K_\phi + K_\phi^2) dA_0 \quad (7c)$$

whereas the energy due to internal gas compressibility and the resulting compression assumes the form:

$$E_c = - \int_{V_0}^V (P_G - P_0) dV \xrightarrow[\text{eq.(2)}]{P_0=P_A} E_c = - P_A V_0 \ln V \Big|_{V_0}^V + P_A (V - V_0),$$

$$\frac{dE_c}{dV} = - \Delta P_G = P_0 - P_G \quad (7d)$$

The latter relation is similar to the one employed by Lipowsky *et al* [23] for vesicles containing liquid solutions, with the understanding that in the present study the initial bubble pressure P_0 is equal to the ambient pressure P_A before application of the overpressure. Since the gas inside the microbubble is compressible, the respective energy variation due to volume changes is determined by the amount by which the internal pressure rises, $P_G - P_0$, as a result of compression. Resistance to compression constitutes an additional stiffness of the microbubble that affects the static response as the external overpressure increases significantly.

The problem formulation is rendered dimensionless by introducing the characteristic length scale, R_0 . Then the solution depends mainly on two dimensionless parameters,

$$\tilde{k}_b = \frac{k_b}{\chi R_0^2}, \quad \tilde{P}_A = \frac{P_A R_0}{\chi}, \quad \chi \equiv 3Gh; \quad (8a)$$

χ signifies the area dilatation modulus of the shell, which is introduced in order to eliminate the shell thickness from the formulation. In this fashion, in cases for which a shell thickness is not easily defined, such as phospholipid monolayer or bilayer shells [24], the bending resistance becomes an independent elasticity parameter [25]. For polymeric shells that normally have thicker coatings, bending resistance is related to the elastic modulus and the shell thickness. Hence,

$$k_b = \frac{3Gh^3}{12(1-\nu^2)} \xrightarrow{\nu=0.5} \tilde{k}_b = \left(\frac{h}{3R_0} \right)^2 \quad (8b)$$

and the ratio between the shell thickness and the microbubble radius emerges as an independent dimensionless number. It should be stressed that the above two parameters, \tilde{k}_b , \tilde{P}_A , denote the relative importance among the three resistances to shell deformation, namely the stretching and bending stiffness of the shell as well as gas compressibility. Finally, an additional dimensionless parameter can be defined, $\Delta\tilde{P} = (\Delta P R_0) / \chi$, as a measure of the intensity of the external disturbance.

3. Numerical solution—validation

The normal and tangential components of the force balance, equation (1), along with the isothermal law describing pressure variations inside the shell (equation (2)), are discretized via the finite element method in order to provide the radial and polar coordinates of the deformed shell. Owing to axisymmetry only the generating curve of the shell surface requires discretization, rendering the numerical problem one dimensional. The equation that fixes the center of mass at the origin of the axis of symmetry, equation (6d), is introduced in place of the tangential force balance at the equator in order to avoid multiple solutions that will arise due to the translational symmetry of the problem formulation. Integration by parts of the integral equations that arise in the process of the finite element discretization affords efficient imposition of the boundary conditions at the two poles, equation (5), that enforce axisymmetry upon the numerical solution.

For example, the normal component of the force balance is recast in spherical coordinates and dimensionless form as:

$$\left(\tilde{P}_G - \tilde{P}_A \right) - \left(k_s \tau_s + k_\phi \tau_\phi \right) + \left(\tilde{k}_b \frac{d}{ds} \left[\frac{d\sigma}{ds} \left(\frac{d}{d\sigma} (\sigma m_s) - m_\phi \right) \right] \right) = \Delta \tilde{P}, \quad \text{with } \sigma = r \sin \theta \quad (9)$$

At equilibrium the externally applied overpressure is balanced by the resistances to compression, elongation and bending signified by the three terms in parenthesis in the above equation.

As can also be gleaned from the above equation, the normal force balance involves second derivatives of the bending moments, m_s , which in their turn involve calculation of the principal curvatures, k_s, k_ϕ . Since the latter also involve evaluation of the second derivatives of the shell coordinates, r, θ , it follows that fourth order derivatives enter the numerical solution. Hence, the finite element methodology with the B -cubic splines, $B_i(\xi)$, as basis functions is employed in order to reduce the smoothness requirements in the weak formulation that arises [26]. Indeed, upon integrating by parts twice and applying the boundary conditions at the two poles, equation (5), the weak formulation of equation (9) becomes:

$$\begin{aligned} 0 = & \int_0^1 B_i r \sin \theta \left(\tilde{P}_A + \Delta \tilde{P} - P_G \right) \frac{ds}{d\xi} d\xi + \int_0^1 B_i \left(k_s \tau_s + k_\phi \tau_\phi \right) r \sin \theta \frac{ds}{d\xi} d\xi \\ & - \int_0^1 \tilde{k}_b \frac{dB_i}{d\xi} \frac{d\xi}{ds} \frac{d\sigma}{d\xi} m_\phi d\xi - \int_0^1 \tilde{k}_b \sigma m_s \frac{d}{d\xi} \left(\frac{dB_i}{d\xi} \frac{d\xi}{ds} \right) d\xi, \\ r(\xi) = & \sum_{i=0}^{N+1} a_i B_i(\xi), \\ \theta(\xi) = & \sum_{i=0}^{N+1} b_i B_i(\xi); \end{aligned} \quad (10)$$

where N denotes the number of elements of the finite element discretization. The tangential component of the force balance is discretized in a similar fashion whereas the isothermal ideal gas law and the positioning of the center of mass are directly applied in their integral dimensionless form:

$$\tilde{P}_A - \tilde{P}_G \int_0^1 \frac{1}{2} r^3 \sin \theta \frac{d\theta}{d\xi} d\xi = 0 \quad (11a)$$

$$(2\pi/4) \int_0^1 r^4 \cos \theta \sin \theta \frac{d\theta}{d\xi} d\xi = 0, \quad (11b)$$

The entire set of equations is treated in the residual form:

$$R_i(r_j, \theta_j, P_G) = 0 \quad i, j = 1, N + 2 \quad (12)$$

and Newton's method is employed for calculating the unknowns $x_i^{k+1} = (r_i^{k+1}, \theta_i^{k+1}, P_G^{k+1})$ at the $(k+1)$ th iteration for given values at the k th iteration:

$$\begin{aligned} J_{ij}(x_i^k) \Delta x_j^k &= R_i^k(x_i^k), \\ \Delta x_i^k &= x_i^k - x_i^{k+1}, \\ J_{ij} &= \frac{\partial R_i}{\partial x_j} \approx \frac{R_i(x_j + \Delta x_j)}{\Delta x_j} \end{aligned} \quad (13)$$

with J denoting the Jacobian matrix. Due to the complexity of the integral forms in equation (10) numerical differentiation was selected for the evaluation of the entries of the Jacobian matrix by calculating the residuals at a fixed increment of x_j , $\Delta x_j = 10^{-8}$, while maintaining the rest of the unknowns at a fixed level. In this fashion, convergence was afforded, with a varying convergence rate depending on the degree of excursion of the solution sought after from the initial guess, when simple continuation is performed [27]. Once a converged solution is obtained the eigenvalues of the Jacobian matrix are calculated and the stability of the deformed shape is investigated. Standard BLAS and LAPACK routines are employed for the inversion and eigenvalue calculation of the Jacobian matrix, which is treated as a full matrix. The stability of a certain branch is determined by the number of negative eigenvalues corresponding to the converged solutions obtained for varying external overpressure. The eigenvectors corresponding to the unstable eigenvalues are calculated so that an initial guess is generated, which, for a suitable disturbance ε on the basic spherical configuration, will provide a large enough geometric imperfection that will direct Newton's iterations towards the emerging subcritical branch [27].

The above methodology was implemented in order to recover bifurcation diagrams available in the literature, for spherical shells that obey Hooke's law. In particular, the case for constant internal pressure reported in [15] is calculated for a shell with radius of $2 \mu\text{m}$ and, thickness $h = 0.2 \mu\text{m}$, shear modulus $G = 88 \times 10^6 \text{ Pa}$ and Poisson ratio $\nu = 0.5$; the corresponding dimensionless parameter values are $\tilde{P}_A = 4 \times 10^{-3}$, $\tilde{k}_b = 10^{-3}$. It should be noted that in the present study the isothermal ideal gas law is employed for capturing pressure variations of the enclosed gas as opposed to fixing the volume or the internal pressure as in [15]. Furthermore, in [15] the shell shapes and stability of the emerging solution branches were obtained via minimization of the total energy as opposed to the solution of the force balance followed by eigenvalue analysis.

Figure 3 illustrates the evolution of the different solution branches in the plane defined by the dimensionless external overpressure, $\Delta \tilde{P}$, and the relative volume change between the deformed and the initial state of the shell, V/V_0 ; a uniform mesh of 200 and 400 B-cubic splines was used for the discretization of the shell surface and agreement was verified between the numerical solution obtained in the present study and in [15]. The numerically obtained diagram confirms that the asymmetric branch emerges first as the dominant instability for $\Delta P = 3.2 \times 10^6 \text{ Pa}$, that is, roughly, 0.92 of the theoretical value

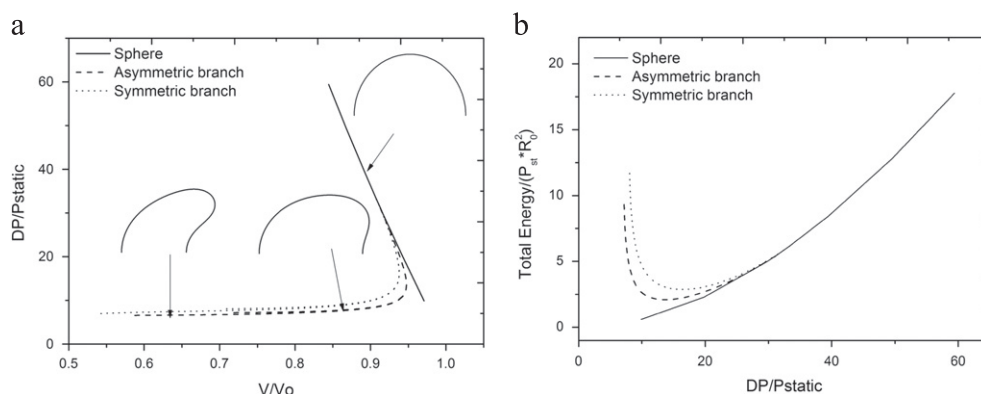


Figure 3. Benchmark calculation of (a) bifurcation diagram and (b) total energy for the case with thickness $h=0.2\ \mu\text{m}$, shear modulus $G=88\times 10^6\ \text{Pa}$, Poisson ratio $\nu=0.5$ and $R_0=2\ \mu\text{m}$. Continuous, dashed and dotted lines correspond to the spherical configuration, asymmetric and symmetric solution families. The shapes shown are obtained at different locations of the asymmetric solution family.

$$\Delta P_{Cr} = \frac{4.3G}{\sqrt{12(1-\nu^2)}} \left(\frac{h}{R_0} \right)^2 \quad (14)$$

obtained from linear stability analysis on the spherical configuration. This is in direct agreement with the critical value taken from a similar diagram in [15]. Furthermore, the secondary bifurcation leading to a symmetric solution family was also recovered. Agreement between the two approaches is justified, despite the different treatment of the internal pressure variation adopted herein, due to the negligible resistance to compression of the microbubble indicated by the very small value of the dimensionless pressure, $\tilde{P}_A = 4 \times 10^{-3}$.

The asymmetric branch is linearly unstable with one negative eigenvalue whereas the symmetric branch that follows is characterized by two negative eigenvalues. Both branches evolve subcritically and they require imposition of a geometric disturbance of a certain amplitude, in the form of the eigenvector provided by stability analysis as was explained above, on the base spherical shape in order to perform parametric continuation on them. The evolution of both branches was followed for a wide range of external overpressures, also in agreement with the above study, and the minimum external overpressure for nonlinear transition to an asymmetric shape to be possible, starting from the spherical configuration, was recovered. It should be noted that the evolution of shapes from the spherical configuration along the asymmetric solution family, exhibits a gradual transition into flattened shapes in the vicinity of the pole followed by dimple formation, see also figure 3, in a fashion that is similar to the response to a point load, shown in the next section. The symmetric solution family also progressively exhibits pronounced dimple formation in the region around the two poles.

4. Results and discussion

Based on the above methodology, an extensive numerical investigation was carried out of the static response of polymeric and phospholipid shells subject to external uniform and point loads. These two types of shells are distinguished by the fact that the former are much stiffer

in terms of both stretching and bending elasticities [11, 12]. Furthermore, they are mostly characterized by Hooke's law [10, 12], whereas phospholipid shells are strain softening for relatively large deformations [11, 12]. In the present study we first examine the response of both types of shells to a uniform external overpressure while using elastic properties that are available from the literature. Next we present results regarding the response of coated microbubbles to a point load distribution and comment on the possibility to obtain estimates of the shell elastic properties based on details of the force–displacement curve. Most of the results presented in the sections below were obtained using 400 elements along the generating curve of the axisymmetric shell, and verified via mesh refinement with 600 elements.

4.1. Uniform external load-bifurcation diagrams

The static response of a polymeric and a phospholipid shell is studied via simple parametric continuation in the parameter space defined by the uniform external overpressure, $\Delta\tilde{P}$, and relative volume change, V/V_0 . To first approximation both types of shells are taken to obey Hooke's law; the Poisson ratio ν is set to 0.5.

In the former case Bisphere is used as the contrast agent coated by a polymeric shell, with indicative elastic constants obtained from the literature [17], $G = 970 \text{ MPa}$, $h = 39 \text{ nm}$, $\nu = 0.42$; $R_0 = 2 \mu\text{m}$. These parameter values correspond to area dilatation modulus and bending stiffness on the order of $\chi = 3$, $Gh = 113 \text{ N m}^{-1}$ and $k_b = 1.7 \times 10^{-14} \text{ N m}$ and consequently the dimensionless parameters governing the microbubble's mechanical response are $\tilde{P}_A = 2 \times 10^{-3}$, $\tilde{k}_b = 0.25 \times 10^{-4}$. As can be gleaned from figure 4, in this case the bifurcation diagram is modified in comparison with figure 3 in the sense that the symmetric solution branch emerges as the primary instability of the basic spherical configuration. Repeating both calculations ignoring pressure changes in the microbubble does not result in any significant changes of the bifurcation diagram. In both cases the resistance to compression due to gas compressibility is small, $\tilde{P}_A \ll 1$, whereas in the case depicted in figure 4 the resistance to stretching dominates over bending resistance to a greater extent, smaller \tilde{k}_b . Hence, the critical overpressure is lower, the volume change at criticality smaller and the results of linear theory closer to the numerically calculated one. The critical external overpressure is almost identical to the prediction of linear theory, $\Delta P_{Cr} \approx 0.83 \text{ MPa}$, and the dominant eigenmode is the 14th Legendre mode, P_{14} , as can be verified by performing Fourier analysis of the numerically calculated dominant eigenvector at the bifurcation point. The emerging solution branch evolves subcritically, it is identified by a single negative eigenvalue and is characterized by shapes that exhibit a progressively more pronounced dimple. Further increase of the external overpressure reveals a second unstable eigenvalue, on the base spherical shape, whose corresponding eigenvector is characterized by an odd Legendre mode, P_{13} . This indicates the onset of an asymmetric solution branch that also emerges subcritically with two negative eigenvalues. Hence, the change in the dimensionless bending resistance in the cases portrayed in figures 3 and 4 results in an exchange in the order of appearance of the first two dominant eigenmodes. In this case it can be argued that for given amount of compression, V/V_0 , as bending resistance decreases bending becomes energetically favorable over stretching and the shell first exhibits two symmetric dimples as opposed to the one in figure 3. Figures 3(b) and 4(b) illustrate the evolution of the total energy pertaining to each one of the solution branches verifying the above assertion. The evolution of the asymmetric branch is captured at its initial stages. However, as the external overpressure decreases beyond a certain value, shapes belonging to the symmetric branch are obtained and the number of negative eigenvalues is reduced to one. It should also be stressed that as the

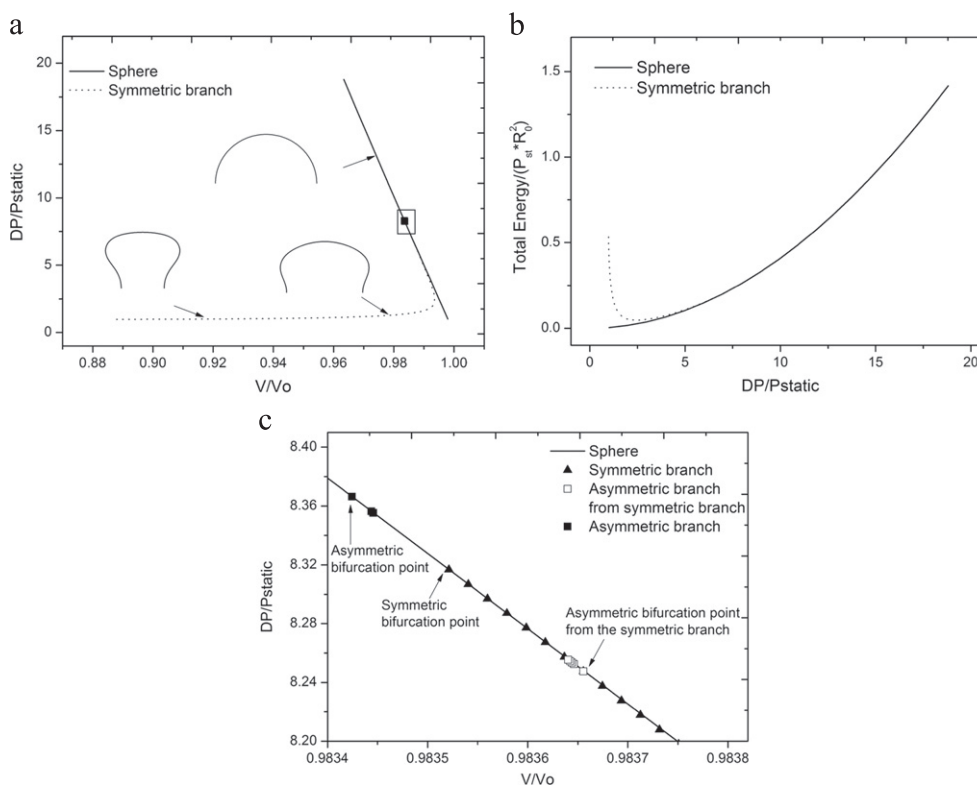


Figure 4. (a) Bifurcation diagram and (b) total energy for a Bisphere microbubble with $G=970$ MPa, $h=39$ nm, $\nu=0.42$ and $R_0=2.6$ μm . Continuous and dashed lines correspond to the spherical configuration and symmetric solution families. The shapes shown are obtained at different locations of the symmetric solution family. (c) Zoom in on the bifurcation diagram in the vicinity of the bifurcation points. Black squares and triangles indicate members of the asymmetric and symmetric branches stemming from the main spherical solution family. Open squares indicate members of the asymmetric solution family that bifurcates from the symmetric branch.

symmetric branch evolves for smaller external overpressures, a secondary bifurcation point appears whose corresponding eigenvector is dominated by P13, it is characterized by asymmetric shapes and possesses two negative eigenvalues, much like the asymmetric branch evolving from the main solution family with spherical shapes. Consequently, for the parameter range pertaining to Bisphere the bifurcation diagram is quite different from the one depicted in figure 3. An exchange in the sequence of the bifurcation points has occurred that favors the onset of symmetric buckled shapes while the asymmetric branch is conjectured to connect the symmetric one with the base solution family of spherical shapes. Figure 4(c), which zooms in the vicinity of the bifurcation points, is an attempt to illustrate this behavior.

An extensive parametric study was performed in order to capture the exchange of stability between the two solution families. Using the parameter set from the benchmark study in figure 3 and gradually reducing the dimensionless bending resistance, \tilde{k}_b , the distance between the two bifurcation points corresponding to the onset of the asymmetric and symmetric branches tends to decrease, table 1, until they overlap with the latter emerging first. Clearly as \tilde{k}_b decreases a threshold value, $\tilde{k}_b < 10^{-6}$, is reached where the two bifurcation points coalesce

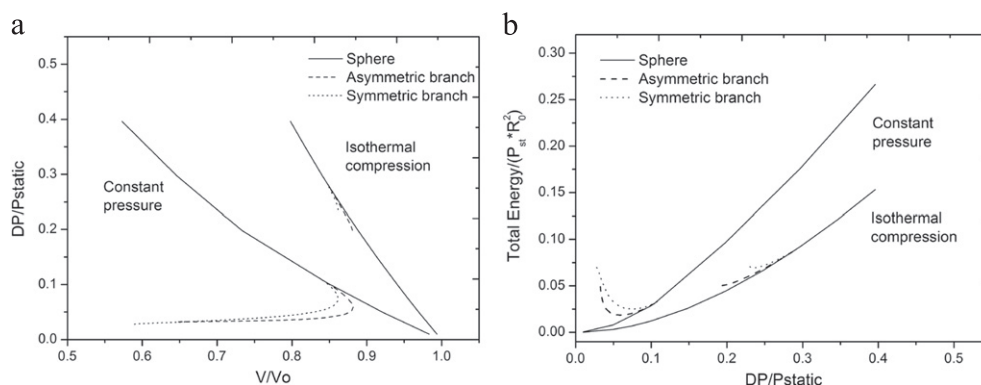


Figure 5. (a) Bifurcation diagram and (b) total energy for a BR14 microbubble with $\chi = 3 Gh = 0.11 \text{ N m}^{-1}$, $k_b = 2.8 \times 10^{-15} \text{ N m}$ and $R_0 = 2.6 \mu\text{m}$. Continuous, dashed and dotted lines correspond to the spherical configuration, asymmetric and symmetric solution families. Families that evolve towards larger external overpressures (smaller total energies) correspond to isothermal compression whereas the ones that evolve towards smaller values (larger total energies) correspond to constant internal pressure calculations.

and the structure of the bifurcation diagram is significantly altered from this threshold value onwards. Capturing the detailed structure of the emerging bifurcation diagram constitutes a difficult task since all branches evolve very near the spherical solution family, figure 4(c), and requires special numerical handling. This is not within the scope of the present study and is left for future investigation.

In order to study the response of phospholipid shells to a uniform load, e.g. BR14, the above calculations are repeated adopting from the literature [28, 29] much smaller values for the stretching and bending stiffness, $\chi = 3 Gh = 0.11 \text{ N m}^{-1}$, $k_b = 2.8 \times 10^{-15} \text{ N m}$, with corresponding dimensionless parameter values, $\tilde{P} = 2.27$, $\tilde{k}_b = 0.004$; $R_0 = 2.6 \mu\text{m}$. In this case both bending stiffness and the stiffness due to gas compressibility are important. It should also be noted that for this type of microbubble the shell thickness is no longer a relevant variable, these are lipid monolayer shells, and the bending stiffness is used as the fundamental property along with the area dilatation modulus. Furthermore, the resistance to compression is of equal importance as the stretching and bending resistances and consequently ignoring it provides a considerably different response pattern, see figures 5(a) and (b).

The critical overpressure required for buckling to take place in this case is significantly larger when the gas compressibility is taken into consideration, see also figure 5. Since the dimensionless bending stiffness is much larger in this case, in comparison with those illustrated in figures 4 and 5, static buckling takes place at a critical overpressure that differs significantly from the prediction of linear theory. This is better understood in terms of the elastic energy distribution among stretching, bending and gas compressibility. Due to the large relative bending stiffness a large amount of volume compression is required before bending becomes energetically favorable over stretching so that buckling takes place, see also figure 5(b). The two solution families, corresponding to the asymmetric and symmetric unstable eigenvector, evolve subcritically towards smaller external overpressures with the asymmetric solution family being the dominant one, figure 5(a), being energetically favored over the symmetric branch, see also figure 5(b), and possessing one negative eigenvalue versus two for the symmetric branch. The shape sequence along this branch follows the

Table 1. Evolution of the numerically evaluated bifurcation point pertaining to the asymmetric and symmetric branches stemming from the spherical solution family, as the relative bending resistance decreases.

\tilde{k}_b	$\tilde{P} = 4 \times 10^{-3}$				
	10^{-3}	10^{-4}	10^{-5}	10^{-6}	10^{-7}
$\Delta\tilde{P}_{cr}$ asym- metric mode	1.280×10^{-1}	4.040×10^{-2}	1.272×10^{-2}	4.020×10^{-3}	1.273×10^{-3}
$\Delta\tilde{P}_{cr}$ sym- metric mode	1.348×10^{-1}	4.080×10^{-2}	1.276×10^{-2}	4.028×10^{-3}	1.272×10^{-3}

schematic presented in figures 1(a)–(c), i.e. the compressed spherical shape becomes flattened at the onset of the solution family while gradually developing a more pronounced dimple around one of the poles. As will be seen in the next subsection, this is a very similar sequence of deformed shapes to the one obtained for the application of a point load on one of the two poles of the microbubble. In particular, transition from the flattened shapes to dimple formation as well as the details of dimple formation itself, contain useful information for estimating the elastic properties of the shell [6, 15, 17, 18].

It should also be stressed that continuation of both branches as the external overpressure decreases does not exhibit the same response as in the case for which gas compressibility is not accounted for, figure 5. In the latter case the microbubble is significantly compressed in this process. Clearly this cannot be the case when the resistance to compression is taken into consideration and the emerging branches follow a different path. To this end a parametric study was conducted using the parameter values employed in figure 3 as starting point and gradually increasing the dimensionless initial internal pressure, \tilde{P}_A . The bifurcation pattern illustrated in figure 3 is recovered, with the asymmetric branch being the dominant instability, until large compression rates are achieved, $V/V_0 < 1$; see also figures 6(a)–(c). It was a recurring theme in this computation that numerical solution became progressively more tedious until, beyond a certain threshold level of compression, a solution could not be obtained. The threshold value in V/V_0 for this critical behavior to be obtained systematically increased as the resistance to compressibility increased with increasing \tilde{P}_A , indicating the fact that compressed states become less favorable. Such numerical difficulties were reported elsewhere in the literature as well [15] for the same type of computation and similar parameter range. In the latter study it was shown that such difficulties arise due to the fact that the shell exhibits regions where opposite sides are in contact for both the asymmetric and symmetric branches. Such shapes appear in order to accommodate higher compression levels and are obtained as the external overpressure is increased away from the problematic region. In the present study the model equations employed for the shell do not allow for such shapes to be captured hence the simulations are stopped beyond a certain compression level, see figures 3(a), 5(a), 6(a)–(c). Further examination of this part of the bifurcation diagram was not pursued in the present study since it is expected that three dimensional wrinkles will arise [10] before the onset of shapes exhibiting contact of opposite sides of the shell.

The effect of the constitutive law on the static response to a uniform external load was examined for contrast agent BR14 assuming a strain softening behavior, setting b parameter to zero, and it was seen that the bifurcation diagram exhibited similar structure as in figure 4 with the symmetric branch becoming the primary instability, figure 7, despite the small value of \tilde{k}_b . This type of response is attributed to the strain softening nature of the shell, which

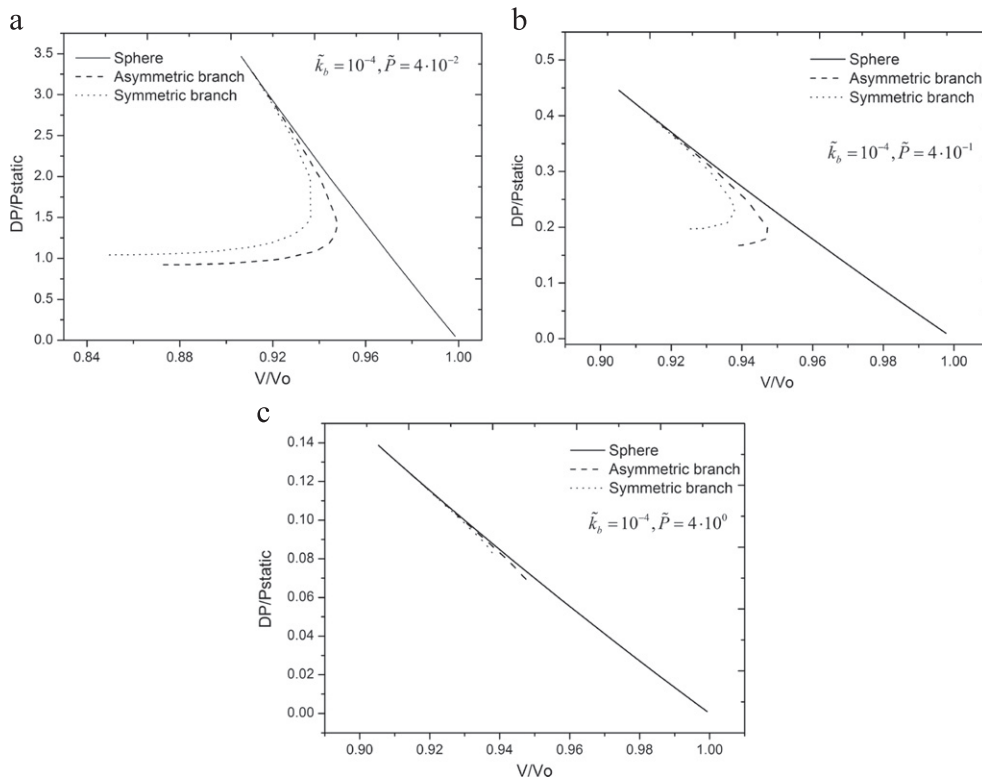


Figure 6. Bifurcation diagrams for microbubbles with the same dimensionless bending modulus and different resistance to gas compression.

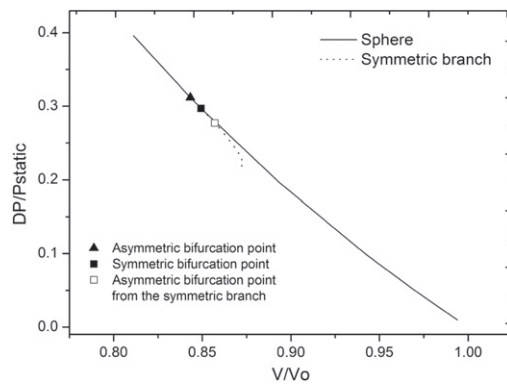


Figure 7. Bifurcation diagram for a BR14 microbubble obeying the Mooney–Rivlin constitutive law. The black square and triangle denote the onset of the symmetric and asymmetric branches, respectively. The empty square denotes the onset of an asymmetric branch off the symmetric solution family.

becomes harder during compression. This, essentially, amounts to the shell exhibiting a larger area dilatation modulus χ than its nominal value used in evaluating \tilde{k}_b . As a result the effective

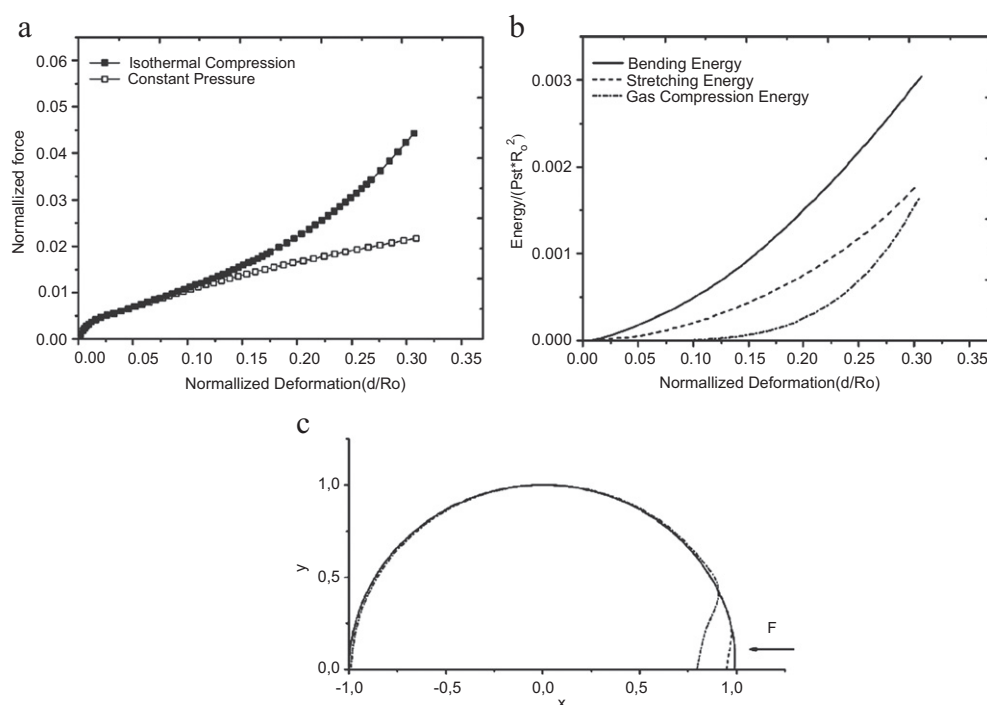


Figure 8. (a) Force–displacement curve and (b) energy distribution for a phospholipid microbubble subject to a point load; $\chi = 3 Gh = 2.4 \text{ N m}^{-1}$, $k_b = 8 \times 10^{-17} \text{ N m}$ and $R_0 = 1.5 \mu\text{m}$. Dark squares denote points obtained with the model that includes isothermal compression. Open squares denote points obtained with the model that assumes constant internal pressure. (c) Numerically obtained shapes along the response curve that includes the effect of compressibility at a normalized deformation of 0.01 (solid line), 0.05 (dashed line) and 0.2 (dashed-dot line).

dimensionless bending resistance $\tilde{k}_{b, \text{Eff}}$ is much smaller than \tilde{k}_b and dimple formation is favoured over stretching of the shell, which explains the onset of symmetric shapes. It should also be stressed that the structure of the bifurcation diagram, including the asymmetric branch off the spherical solution family and the secondary asymmetric bifurcation from the symmetric branch, is very similar to the case shown in figures 4(a)–(c) where also the symmetric mode emerges before the asymmetric branch, figure 7.

4.2. Point load-parameter estimation

In order to assess the response to a point load distribution we examine the response of a coated microbubble with elastic properties $\chi = 3 Gh = 2.4 \text{ N m}^{-1}$, $k_b = 8 \times 10^{-17} \text{ N m}$ and corresponding dimensionless parameters $\tilde{P} = 0.06$, $\tilde{k}_b = 1.5 \times 10^{-5}$; $R_0 = 1.5 \mu\text{m}$. Figure 8(a) illustrates the response of the microbubble in the form of a force deformation curve. The deformation, Δ , is indicatively calculated at the pole where the point load is applied and the force, F , is the integral of the external load, point load in this case, over the deformed shell surface. The response curve is characterized by three distinct regimes with specific features each. As can be gleaned upon comparing the schematics from figure 1, the shapes corresponding to the asymmetric solution families in figures 3(a) and 5(a) and the

shapes from figure 8(c), all conform to the pattern of an initially spherical configuration becoming progressively flatter at the pole until dimple formation takes place.

At very small deformations the response curve exhibits a linear regime that is characterized by flattened shapes around the location of the point load, figure 8(a): this is the classic Reissner regime where a linear relationship exists [30] in the form

$$F = \frac{4\chi}{3\sqrt{3}(1-v^2)\tilde{k}_b}\Delta \quad (15)$$

with F, Δ dimensional. Elastic energy in terms of bending and stretching determines this type of shape with bending being evenly distributed along the flattened part of the shell, figure 8(c). Owing to the small bending stiffness a transition is observed for quite small deformations in the response curve, to a nonlinear force deformation regime where bending is mainly restricted to the two dimple edges, identifying the rim of the dimple that is formed in the vicinity of the point load, see the shape from figure 8(c) pertaining to this regime. Furthermore, this regime is characterized by a nonlinear force deformation law [5]

$$F = \sqrt{\frac{36(1-v^2)\chi k_b \sqrt{\tilde{k}_b}}{R_0}} \sqrt{\Delta} \quad (16)$$

and will be referred to as Pogorelov regime. Typically, Reissner's law is employed for providing estimates of the shell elastic modulus based on AFM measurements [6, 17], but this process relies upon previous knowledge of the shell thickness. This is normally easily recovered for relatively large shells but in the case of coated microbubbles, especially phospholipids, this may not be the case. Hence, it will be useful to combine the two regimes in order to obtain an estimate of the shell thickness and area dilatation modulus at the same time. As the applied point load further increases the volume of the microbubble is compressed to a non-negligible extent, the internal pressure increases and the actual resistance to compression increases as well. As a result the part of the energy stored in the form of gas compression assumes a more important role in the mechanics of deformation, figure 8(b), and this is also reflected in the force deformation curve that now is curved upwards, figure 8(a), indicating this additional stiffness component.

The response pattern registered in figure 8 persists for a wide range of elastic parameters, corresponding to polymeric or phospholipid shells, with the understanding that certain polymeric shells, for which normally resistance to compression is negligible, do not always exhibit the part of the curve that is curved upwards. In fact, on certain occasions [18] this part is superseded by a plateau upon which small scale variations of the measured force appear, possibly as a result of an instability, or even multiplicity of responses is observed. Experimental observations [18] associate this response with an increase in the cantilever stiffness or to a 3D buckling event of the interrogated microbubble. In the first case the cantilever–microbubble interaction should be examined more carefully in order to provide load distributions, especially for flat cantilevers, that are closer to reality. On the other hand, for 3D instabilities to be examined, the numerical methodology has to be extended in order to capture non-axisymmetric shells. In an effort to obtain a simple correction to the response curve for a point load distribution, the response of a coated microbubble is studied subject to the Hertz distribution, equation (6c). In this case the total applied force is known and the angle of contact θ_c is part of the numerical solution. Thus, two independent solutions are obtained, figures 9(a), (b), with the first one corresponding exactly to the solution for a point load, the angle of contact θ_c is vanishingly small, while the other one recovers the spherical shape with

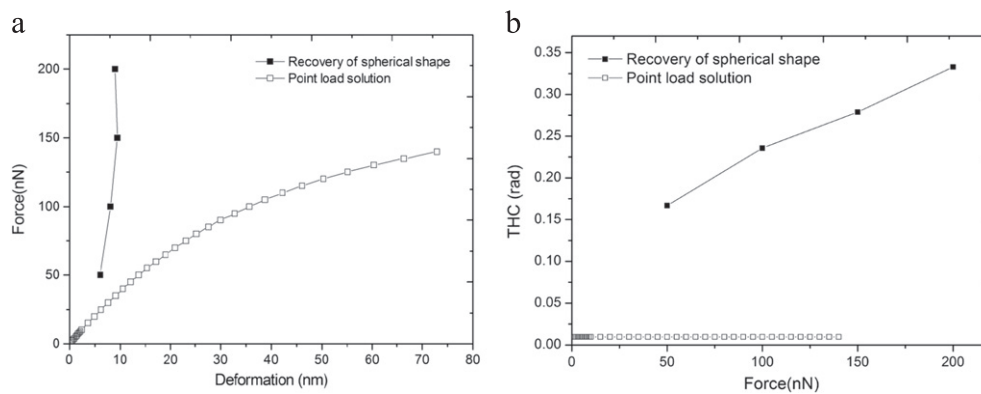


Figure 9. (a) Force–deformation curve and (b) contact angle, as a function of the external load when a Hertzian load distribution is considered; $G = 970$ MPa, $h = 39$ nm, $\nu = 0.42$ and $R_0 = 2.6$ μ m.

a gradually increasing angle of contact, figure 9(b). These two solutions correspond to the two extremes of the cantilever and the microbubble controlling the stiffness of the system. Clearly a better model of the cantilever–microbubble interaction is required if the issue of multiplicity is to be addressed in the microbubble response, and is left to a future study.

In a similar context, it has been observed experimentally [19] that phospholipid shells do not always follow Reissner’s law at small deformations. This type of behavior is normally observed at very small forces, on the order of several nN, in which case a nonlinear response curve is obtained even for very small deformations. In this case it is possible that intermolecular forces dominate the microbubble response, associated with attraction or repulsion between the shell material and the cantilever. In either case a nonlinear response curve is expected [3] corresponding to the dominant effect of surface energy. In such a situation transition from Reissner to Pogorelov type response in the force–deformation curve may not be useful in estimating shell parameters. Rather the second transition, the one associated with the curved upwards part of the response curve, corresponding to the transition from bending dominated behavior, as in the Pogorelov regime, to gas compressibility control, as in the final part of the response curve, can be used in order to obtain useful estimates pertaining to the elastic behavior of the shell.

5. Conclusions

The static response of a coated microbubble subject to different external load distributions was investigated numerically. Comparison against theoretical predictions and benchmark parametric studies were conducted that accurately reproduced available data from the literature.

Bifurcation diagrams were constructed for contrast agents with polymeric, Bisphere, and phospholipid coatings, BR14. Parametric continuation was performed in the parameter space defined by the \tilde{k}_b , \tilde{P}_A , parameters measuring the relative importance of bending and compression stiffness with respect to stretching. In the case of Bisphere the dimensionless bending stiffness is much smaller than the one used in the benchmark study causing an exchange in the sequence of bifurcations on the spherical solution family leading to deformed shapes, with the symmetric branch taking precedence as the dominant instability over the

asymmetric one while both branches evolve subcritically. This is conjectured to be the result of a mode coalescence event as the two bifurcation points coincide. In the parameter range beyond this coalescence the bifurcation diagram changes. The asymmetric branch evolves over a small interval of external overpressures and is conjectured to terminate on the symmetric branch in the form of an additional bifurcation point that appears on the symmetric branch and is also asymmetric in nature. The relative resistance to compression is very small in this case and consequently allowing for isothermal pressure variations inside the microbubble bears no significance on the static response.

Bifurcation diagrams pertaining to BR14 were also constructed and they are characterized by the large resistance to compression. The bifurcation structure is similar to the one obtained in the benchmark case with the asymmetric and symmetric branches terminating at larger final to initial volume ratios, V/V_0 , indicating the resistance of the shell to additional compression. Both branches are expected to be complemented by a solution family exhibiting contact between opposite ends, in the manner obtained elsewhere [15] with the new solution family turning to larger external overpressures while achieving smaller V/V_0 ratios, but this transition will take place at smaller threshold compression levels, larger V/V_0 , as the relative resistance to compression, \tilde{P}_A , increases. Such a transition is, however, not expected to persist in the presence of three dimensional disturbances. It should also be stressed that accounting for nonlinearity in the constitutive law, i.e. introducing strain softening behavior to BR14, leads to an increased effective stretching resistance during compression that amounts to a reduction in the relative bending resistance, \tilde{k}_b , thus forcing the symmetric solution family to supercede the asymmetric branch. The structure of the bifurcation diagram is similar to the one exhibited by Bisphere where also the symmetric branch was seen to bifurcate first off the main spherical solution family.

The response of a coated microbubble to a point force was also investigated as a first step to simulate AFM measurements. The two pressure models pertaining to constant internal pressure and isothermal pressure variation were compared and the response was almost identical for small deformations, but different at large deformations. The pressure model which considers isothermal variations of the internal pressure requires higher forces for the same deformation than the constant pressure model, leading to a curved upwards response curve. Both models exhibit a first linear response identified as the Reissner regime followed by a nonlinear curved downwards part identified as Pogorelov's regime. Asymptotic fitting of the measured static response in these two regimes constitutes a useful tool for estimation of the area dilatation and bending modulus. Extensive data analysis is underway in order to validate this approach and provide a useful interpretation for deviations from this pattern reported in AFM measurements of phospholipid and polymeric shells at very small and large deformations, respectively.

Acknowledgement

This work was performed in the framework of the operational program: "Education and lifelong learning-Aristeia" and is cofounded by the European Union (European Social Fund) and national resources.

References

- [1] Timoshenko S P and Woinowsky-Krieger S 1959 *Theory of Plates and Shells* (New York: McGraw-Hill)

- [2] Landau L D and Lifshitz E M 1986 *Theory of Elasticity* (Butterworth-Heinemann)
- [3] Koga T and Hoff N J 1969 The axisymmetric buckling of initially imperfect complete spherical shells *Int. J. Solids Struct.* **5** 679–97
- [4] Reissner E 1946 Stresses and small displacements of shallow spherical shells I and II *J. Math. Phys.* **25** 279–300
- [5] Pogorelov A V 1988 *Bendings of Surfaces and Stability of Shells* (Providence, RI: American Mathematical Society)
- [6] Fery A and Weinkamer R 2007 Mechanical properties of micro- and nanocapsules: single-capsule measurements *Polymer* **48** 7221–35
- [7] Kaufmann B A, Wei K and Lindner J R 2007 Contrast echocard *Curr. Probl. Cardiology* **32** 51–96
- [8] Ferrara K, Pollard R and Borden M 2007 Ultrasound microbubble contrast agents: fundamentals and application to gene and drug delivery *Annu. Rev. Biomed.* **9** 415–47
- [9] Klibanov A L 2005 Ligand-carrying gas-filled microbubbles: ultrasound contrast agents for targeted molecular imaging *Bioconjugate Chem.* **16** 9–17
- [10] Marmottant P, Bouakaz A, de Jong N and Quilliet C 2011 Buckling resistance of solid shell bubbles under ultrasound *J. Acoust. Soc. Am.* **129** 1231–9
- [11] Paul S, Katiyar A, Sarkar K, Chatterjee D, Shi W T and Forsberg F 2010 Material characterization of the encapsulation of an ultrasound contrast microbubble and its subharmonic response: strain-softening interfacial elasticity model *JASA* **127** 3846–57
- [12] Tsigklifis K and Pelekasis N A 2013 Simulations of insonated contrast agents: saturation and transient break-up *Phys. Fluids* **25** 032109
- [13] Barthes-Biesel D, Diaz A and Dhenin E 2002 Effect of constitutive laws for two-dimensional membranes on flow-induced capsule deformation *J. Fluid Mech.* **460** 211–22
- [14] Tsigklifis K and Pelekasis N A 2008 Nonlinear oscillations of encapsulated microbubbles subject to ultrasound: the effect of membrane constitutive law *J. Acoust. Soc. Am.* **123** 4059–70
- [15] Knoche S and Kierfeld J 2011 Buckling of spherical capsules *Phys. Rev. E* **84** 046608
- [16] Vella D, Ajdari A, Vaziri A and Boudaoud A 2011 Wrinkling of pressurized elastic shells *Phys. Rev. Lett.* **107** 174301
- [17] Glynos E, Sboros V and Koutsos V 2009 Polymeric thin shells: measurement of elastic properties at the nanometer scale using atomic force microscopy *Mater. Sci. Eng. B* **165** 231–4
- [18] Glynos E, Koutsos V, McDicken W N, Moran C M, Pye S D, Ross J A and Sboros V 2009 Nanomechanics of biocompatible hollow thin-shell polymer microspheres *Langmuir* **25** 7514–22
- [19] Santos E B, Morris J K, Glynos E, Sboros V and Koutsos V 2012 Nanomechanical properties of phospholipid microbubbles *Langmuir* **28** 5753–60
- [20] Lulevich V V, Andrienko D and Vinogradova O I 2004 Elasticity of polyelectrolyte multilayer microcapsules *J. Chem. Phys.* **120** 3822–6
- [21] Libai A and Simmonds J G 2005 *The Nonlinear Theory of Elastic Shells* (Cambridge: Cambridge University Press)
- [22] Pozrikidis C 2001 Effect of membrane bending stiffness on the deformation of capsules in simple shear flow *J. Fluid Mech.* **440** 269–91
- [23] Lipowsky R, Brinkmann M, Dimova R, Franke T, Kierfeld J. and Zhang X 2005 Droplets, bubbles, and vesicles at chemically structured surfaces *J. Phys.: Condens. Matter.* **17** S537–58
- [24] Skalak R, Tozeren A, Zarda R P and Chien S 1973 Strain energy function of red blood cell membranes *Biophys. J.* **13** 245–64
- [25] Zarda R P, Chien S and Skalak R 1977 Elastic deformations of red blood cells *J. Biomech.* **10** 211–21
- [26] Pelekasis N A, Tsamopoulos J A and Manolis G D 1990 Equilibrium shapes and stability of charged and conducting drops *Phys. Fluids A* **2** 1328
- [27] Seydel R 1988 *From equilibrium to chaos Practical Bifurcation and Stability Analysis* (Amsterdam: Elsevier)
- [28] van der Meer S M D, Voormolen M M, Chin C T, Bouakaz A, De Jong N, Versluis M and Lohse D 2007 Microbubble spectroscopy of ultrasound contrast agents *JASA* **121** 648–56
- [29] Tsigklifis K and Pelekasis N 2011 Parametric stability and dynamic buckling of an encapsulated micro-bubble subject to acoustic disturbances *Phys Fluids* **23** 012102
- [30] Reissner E 1946 Stresses and small displacements of shallow spherical shells I and II *J. Math. Phys.* **25** 279–300

- [31] Johnson K L, Kendall K and Roberts A D 1971 Surface energy and the contact of elastic solids
Proc. R. Soc. Lond. A **324** 301–13